vectors, according to Eq. (5), are

$$2\,\tilde{e}_{\alpha\beta} = \tilde{G}_{\alpha\beta} - g_{\alpha\beta} \tag{6a}$$

(at T^* resulting from path $Q^* - U^* - T^*$)

$$\tilde{\rho}_{\alpha\beta} = \tilde{B}_{\alpha\beta} - b_{\alpha\beta} \tag{6b}$$

and

$$2\,\hat{e}_{\alpha\beta} = \hat{G}_{\alpha\beta} - g_{\alpha\beta} \tag{7a}$$

(at T^* resulting from path $Q^* - V^* - T^*$)

$$\hat{\rho}_{\alpha\beta} = \hat{B}_{\alpha\beta} - b_{\alpha\beta} \tag{7b}$$

The membrane and bending strains at point T^* should be equivalent regardless of the path from Q^*. Thus, equating the membrane and bending strains of Eqs. (6) and (7),

$$\tilde{e}_{\alpha\beta} = \hat{e}_{\alpha\beta} \tag{8}$$

$$\tilde{\rho}_{\alpha\beta} = \hat{\rho}_{\alpha\beta} \tag{9}$$

By using Eq. (4) and the appropriate base vectors, Eqs. (8) and (9) become

$$\tilde{X}_{\alpha}{}^{i}\tilde{X}_{\beta}{}^{i} = \hat{X}_{\alpha}{}^{i}\hat{X}_{\beta}{}^{i} \tag{10}$$

$$\tilde{X}^{i}{}_{\alpha|\beta}\hat{N}^{i} = \hat{X}_{\alpha|\beta}{}^{i}\hat{N}^{i} \tag{11}$$

Adding $-\tilde{X}_{\alpha}{}^{i}\hat{X}_{\beta}{}^{i}$ to both sides of Eq. (10) and rearranging,

$$(\tilde{X}_{\alpha}{}^{i} + \hat{X}_{\alpha}{}^{i})(\tilde{X}_{\beta}{}^{i} - \hat{X}_{\beta}{}^{i}) = 0 \tag{12}$$

Equation (12) implies

$$\tilde{X}_{\beta}{}^{i} = \hat{X}_{\beta}{}^{i} \tag{13}$$

Thus, Eq. (11) reduces to

$$\tilde{N}_{i} = \hat{N}_{i} \tag{14}$$

Equations (13) and (14) are statements of the strain compatibility conditions in a broad sense. It is necessary, however, to determine the meaning of these equations in terms of the base vectors at point Q^* on S^*. To accomplish this, the base vectors $\tilde{N}_i$, $\tilde{X}_{\alpha}{}^{i}$ and $\hat{N}_i$, $\hat{X}_{\alpha}{}^{i}$ will be written in terms of the base vectors at Q^* by means of a second-order Taylor's expansion. The expansion of the base vectors at Q^* will be made along one surface coordinate curve, ξ^ρ, while ξ^λ is constant ($\xi^\rho \neq \xi^\lambda$). Then, an expansion will be made along the surface coordinate curve ξ^λ, while ξ^ρ is held constant ($\xi^\rho \neq \xi^\lambda$). This process would correspond to the path $Q^* - U^* - T^*$ shown in Fig. 1. The path $Q^* - V^* - T^*$ on S^* would involve a Taylor's expansion along ξ^λ, holding $\xi^\rho =$ const. ($\xi^\lambda \neq \xi^\rho$); then along ξ^ρ, holding ξ^λ constant. Thus, the two sets of base vectors at T^* are given by

$$\begin{aligned}\tilde{X}^{i}{}_{\alpha} = X^{i}{}_{\alpha} + X^{i}{}_{\alpha|\rho}d\xi^{\rho} + X^{i}{}_{\alpha|\lambda}d\xi^{\lambda} + \tfrac{1}{2}!X^{i}{}_{\alpha|\lambda\lambda}(d\xi^{\lambda})^{2} + \\ X^{i}{}_{\alpha|\lambda\rho}d\xi^{\lambda}d\xi^{\rho} + \tfrac{1}{2}!X_{\alpha|\rho\rho}{}^{i}(d\xi^{\rho})^{2}\end{aligned} \tag{15}$$

$$\begin{aligned}\hat{X}^{i}{}_{\alpha} = X^{i}{}_{\alpha} + X^{i}{}_{\alpha|\lambda}d\xi^{\lambda} + X^{i}{}_{\alpha|\rho}d\xi^{\rho} + \tfrac{1}{2}!X^{i}{}_{\alpha|\rho\rho}(d\xi^{\rho})^{2} + \\ X^{i}{}_{\alpha|\rho\lambda}d\xi^{\rho}d\xi^{\lambda} + \tfrac{1}{2}!X_{\alpha|\lambda\lambda}{}^{i}(d\xi^{\lambda})^{2}\end{aligned} \tag{16}$$

$$\begin{aligned}\tilde{N}_{i} = N_{i} + N_{i|\lambda}d\xi^{\lambda} + N_{i|\rho}d\xi^{\rho} + \tfrac{1}{2}!N_{i|\rho\rho}(d\xi^{\rho})^{2} + \\ N_{i|\lambda\rho}d\xi^{\lambda}d\xi^{\rho} + \tfrac{1}{2}!N_{i|\lambda\lambda}(d\xi^{\lambda})^{2}\end{aligned} \tag{17}$$

$$\begin{aligned}\hat{N}_{i} = N_{i} + N_{i|\rho}d\xi^{\rho} + N_{i|\lambda}d\xi^{\lambda} + \tfrac{1}{2}!N_{i|\lambda\lambda}(d\xi^{\lambda})^{2} + \\ N_{i|\rho\lambda}d\xi^{\rho}d\xi^{\lambda} + \tfrac{1}{2}!N_{i|\rho\rho}(d\xi^{\rho})^{2}\end{aligned} \tag{18}$$

The quantities $(\quad)_{|\rho}$ and $(\quad)_{|\rho\lambda}$ are first- and second-order tensor derivatives. Substituting Eqs. (15) and (16) into Eq. (13) and simplifying,

$$X^{i}{}_{\alpha|\rho\lambda} = X^{i}{}_{\alpha|\lambda\rho} \tag{19}$$

Similarly, substituting Eqs. (17) and (18) into Eq. (14), the conditions for bending strain compatibility are

$$N_{i|\rho\lambda} = N_{i|\lambda\rho} \tag{20}$$

Equations (19) and (20) are equivalent to the equations of strain compatibility given by Gol'denveizer on pp. 55–59 of Ref. 2. By using these equations, three independent relationships are obtained. These can be written in the form

$$\epsilon^{\gamma\alpha}\epsilon^{\lambda\rho}[\Gamma_{\gamma\alpha\rho,\lambda} + \Gamma^{\sigma}{}_{\gamma\rho}[\Gamma_{\sigma\alpha\lambda} + B_{\gamma\rho}B_{\alpha\lambda}] = 0 \tag{21}$$

$$\epsilon^{\lambda\rho}B_{\gamma\lambda|\rho} = 0 \tag{22}$$

where $\Gamma_{\gamma\alpha\rho}$ and $\Gamma_{\gamma\rho}{}^{\sigma}$ are the Christoffel symbols of the first and second kinds, respectively, for the deformed surface.

Equations (21) and (22) are the Gauss and Mainardi-Codazzi conditions, respectively. By using Eqs. (7) and the definitions of the Christoffel symbols, these equations can be transformed into the general nonlinear strain compatibility conditions for a shell surface. This procedure is discussed in Ref. 4 and will not be repeated here.

Concluding Remarks

By requiring the measures of the membrane and bending strains to be independent of the natural paths from point to point on the deformed reference surface, the shell compatibility conditions can be derived in a straightforward manner. This derivation has the advantage of being based upon physical arguments rather than wholly mathematical constraints as in other papers. Indeed these mathematical constraints, which have served as the basis for the strain compatibility equations in the past, are obtained directly from this derivation.

References

[1] Odqvist, F., "Equations Complètes de l'Equilibre des Couches Minces Elastiques Gauches," *Comptes Rendus Hebdomadaires des Seances de l'Academie des Sciences*, Vol. 205, 1937, pp. 271–273.

[2] Gol'denveizer, A. L., *Theory of Elastic Thin Shells*, International Series of Monographs on Aeronautics and Astronautics, Pergamon Press, New York, 1961.

[3] Naghdi, P. M., *Progress in Solid Mechanics*, Vol. IV, 1963, pp. 34–39.

[4] Koiter, W. T., "On the Nonlinear Theory of Thin Elastic Shells," *Jaabock Proceedings, Series B: Physical Sciences*, Akademie van Wetenschappen, Amsterdam, Vol. 69, 1966, pp. 1–54.

[5] Leonard, R. W., "Nonlinear First Approximation Thin Shell and Membrane Theory," Ph. D. thesis, June 1961, Virginia Polytechnic Institute.

[6] Sokolnikoff, I. S., *Tensor Analysis Theory and Applications to Geometry and Mechanics of Continua*, 2nd ed., Wiley, New York, 1961, p. 102.

Nucleating Mechanism for Spall in Aluminum

ROBERT H. C. AU*
Lockheed Missiles & Space Company, Sunnyvale, Calif.

SPALL in solids, defined as a complete or partial separation of material resulting from the tension induced by the interaction of two rarefaction waves can be experimentally studied using the gas gun. Gas guns such as those in Ref. 1 use a projectile to carry a flat flyer plate which impacts on a target. Recovery of the target for detailed examination becomes difficult because of the destruction or damage to the target after flyer plate-target impact. A scheme† to eliminate the damage after impact is shown in Fig. 1. The flyer plate is designed to break away from the piston at impact and pass over the sting. The aluminum foam with its low impedance will attenuate the transmitted wave and crush it to a

---

Received January 19, 1970.

* Staff Engineer.

† The author would like to acknowledge A. D. Wood for the development of this scheme.

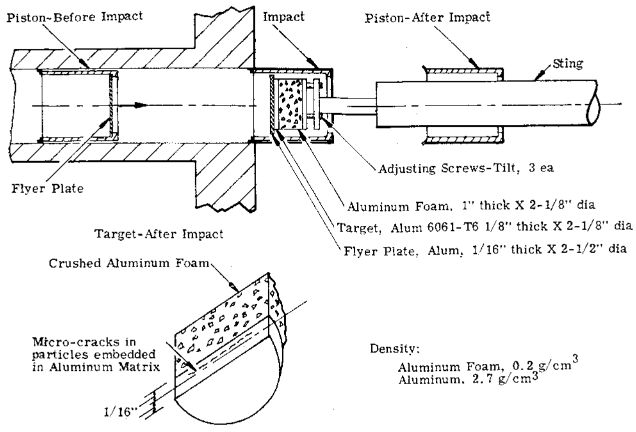

Fig. 1 Schematic of spall experiment apparatus.

nearly uniform thickness due to momentum transfer of the flyer plate. The piston is driven by atmosphere pressure into an evacuated tank that houses the rigidly mounted sting. Velocities as low as 0.035 km/sec have been obtained by this gun and velocities lower than 0.017 km/sec can be achieved. The low-velocity capability together with the break-away piston is very useful for spall assessment and also for equation-of-state characterization of nonmetallic target specimens such as the phenolics. This Technical Note presents the results of an experiment on 6061-T6 aluminum to investigate the mechanism for spall. The results indicate that the nucleating mechanism for spall are micro-cracks which occur in the particles embedded in the aluminum matrix.

Experiment and Results

A 6061-T6 aluminum target, $2\frac{1}{8}$ in. diam by $\frac{1}{8}$ in. thick was impacted by a $2\frac{1}{2}$ in. diam by $\frac{1}{16}$-in.-thick flyer plate (see Fig. 1). The flyer plate velocity, measured by grounding pins, was 0.18 km/sec and corresponds to a calculated compressive stress of about 14 kilobar (kb), (kb = 10^6 dynes/cm^2). Reported spall stress level for this aluminum has been measured by Blincow and Keller.[2] Their results, shown in Fig. 2 indicate a time-dependency for spall in aluminum. They found that by keeping the ratio of the flyer plate thickness to the target thickness constant for a series of impact at constant flyer plate velocity the duration of the stress pulse could be scaled (neglecting strain-rate effects). Blincow and Keller showed that spall (a separation of the aluminum as seen by the naked eye) is not observed if the flyer plate is less than a certain thickness for a given flyer plate velocity. For this experiment, no spall (visible to the naked eye) was observed in the aluminum target which was consistent with the results of Blincow and Keller.

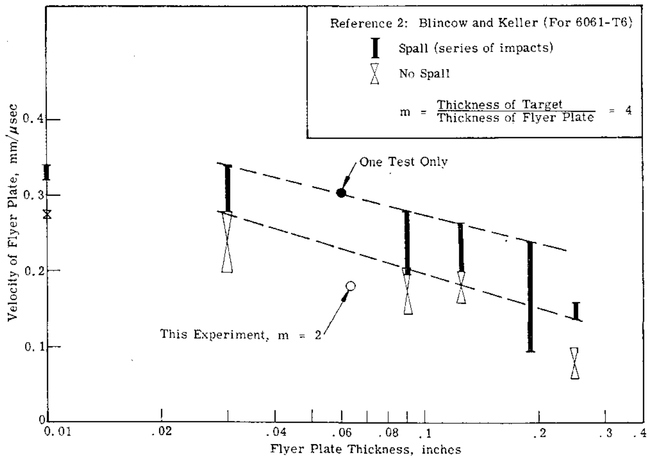

Fig. 2 Data from spall experiments.

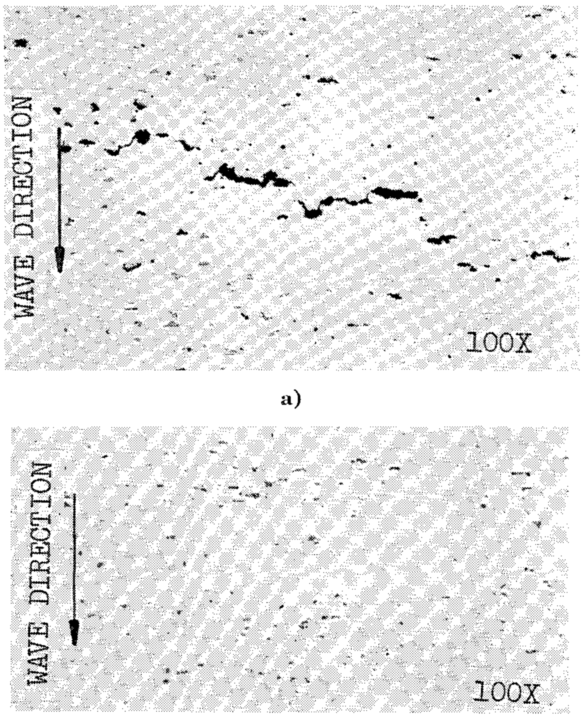

a)

b)

Fig. 3 Photograph of stressed a) and unstressed b) region at 100× magnification.

Since the target was recovered in tact, a further detailed examination of a cut cross-section was made of the stressed region. The target was cut along a diameter and its cross section polished. It was not etched. Photographs of the region magnified 100×, 800×, and 3000× were taken which revealed micro-cracks along particles embedded in the aluminum matrix. Figure 3a shows a 100× magnified view of the specimens cross section which was not subjected to the rarefaction wave interactions. The longitudinal micro-cracks shown in Fig. 3b were confined in a narrow region along the back half of the target and aligned parallel to the front of the stress wave. This behavior is expected since the target was twice as thick as the flyer plate and agrees with the stress wave calculations which show that the interaction of the two rarefaction waves should occur within the back region but near the mid-thickness plane. Photographs of 3000× magnification were also made and one of them is shown in Fig. 4. The spalled particle is clearly seen. However, the adjacent particle and the aluminum matrix has not spalled.

Discussion and Conclusions

Butcher et al.[3] state that fractures may be nucleated at precipitates (particles) as interfacial contact between the matrix and particle is destroyed by shock-wave action. The photograph of Fig. 4 clearly indicates that the initial nucleation of spall probably begins within the particles themselves. Other 3000× magnification photographs taken also show the micro-cracks occurring in the particles and with some extending to the interfacial boundaries.

The break-away piston allows one to eliminate the damage to the target after impact. Examination of the target becomes straightforward and interpretation of the structure of the spall can be made with confidence. With this scheme, it has been shown that the nucleating mechanism for spall in 6061-T6 aluminum is due to micro-cracks in the particles embedded in the aluminum matrix. These micro-cracks are induced by the interaction of two rarefaction waves.

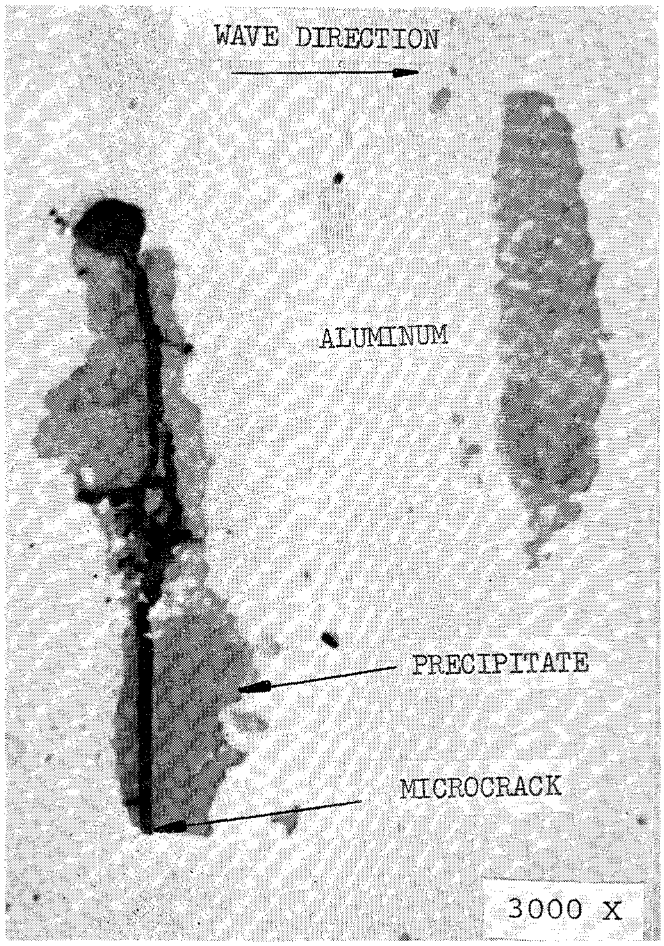

Fig. 4 Photograph of micro-crack in particle embedded in aluminum matrix.

References

[1] Lundergan, C. D. and Herman, W., "Equation of State of 6061-T6 Aluminum at Low Pressures," *Journal of Applied Physics*, Vol. 34, No. 7, July 1963, pp. 2046–2052.

[2] Blincow, D. W. and Keller, D. V., "Experiments on the Mechanism of Spall," *Dynamic Behavior of Materials*, American Society for Testing Materials, Philadelphia, Pa., 1963, pp. 252–263.

[3] Butcher, B. M. et al., "Influence of Stress History on Time-Dependent Spall in Metals," *AIAA Journal*, Vol. 2, No. 6, June 1964, pp. 977–990.

Vortices in Separated Flows

Allen H. Whitehead Jr.[*]
NASA Langley Research Center, Hampton, Va.

SEVERAL experimentalists[1–3] have shown that vortices existing in separated flows can result in a variation in the properties in the spanwise direction. The experimental evidence of Ginoux[1] and Roshko and Thomke[2] indicated the presence of vortices in the vicinity and downstream of reattachment. The experiment of Reding et al.[3] on a cone-cylinder-flare configuration with local transonic conditions verified the existence of vortices and a strong circulatory flow within a transitional-separated region; the resulting separation and reattachment points varied widely around the circumference. These observed variations have led Reding et al.[3] to conclude that the assumption of axisymmetric separated flow is unrealistic. Evidence of symmetric separation is presented in the present Note which indicates that Reding's conclusion is not universally valid. The role of vortices in separated flows is also examined.

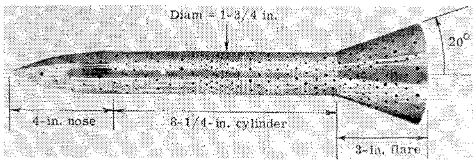

Fig. 1 Model dimensions and oil-dot pattern prior to run. Dimensions in inches.

An experimental study was conducted at Mach 6.8 in the Langley 11-in. tunnel at a unit Reynolds number of 0.33×10^6 per in. on a model similar to that employed by Reding, but with the conical nose replaced by an ogive nose. The schlieren pictures indicate that transition occurs within the separated region just downstream of the cylinder-flare juncture. The transition position and separated-flow characteristics in the present tests are compatible with previous results on geometrically similar models run in the same facility.[4] Figure 1 shows the model dimensions and illustrates the oil-dot technique employed in the study; the dots are composed of a mixture of oil and lampblack, and have been placed on the model in a systematic manner with a higher density of dots in the anticipated areas of separation and reattachment.

Three views of the oil-flow photographs from this investigation are shown in Fig. 2. The separation and reattachment regions as indicated by the oil flow show that the separated flow is symmetrical about this configuration. There is no indication of the large circumferential circulation in the plane of the body symmetry reported by Reding. Similar symmetric characteristics were observed in oil flow studies of turbulent separation over a cylinder and 40° flare studied by Polak at Mach 5, 6, and 7.[5] Polak's oil flow results were part of a larger study to examine separation-length characteristics at high Reynolds numbers.[6]

The asymmetric separation observed by Reding et al.[3] at zero angle of attack could be atrributed to several factors such as 1) the general unsteadiness that is characteristic of transonic flows and 2) the occurrence of a transitional-separated boundary layer. Chapman[7] has shown that for flat-plate transitional separation, the transition position is sensitive to a Reynolds number variation. As a result, the characteristics of the transitional-separated region are likewise sensitive to small changes in surface and flowfield properties. In contrast, laminar, and turbulent separations are known to be far

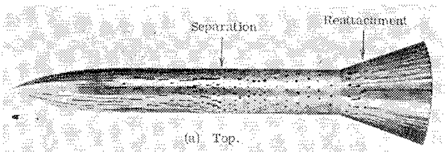

(a) Top.

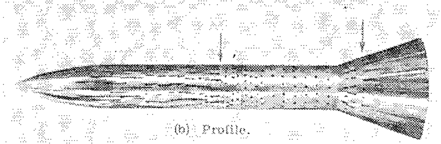

(b) Profile.

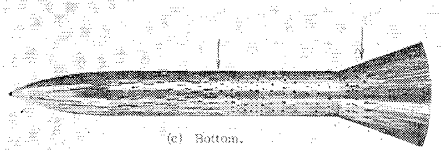

(c) Bottom.

Fig. 2 Oil-flow pictures at $\alpha = 0°$; $M_\infty = 6.8$; R_∞/in. = 0.33×10^6.

Received February 18, 1970.

[*] Aerospace Engineer, Applied Fluid Mechanics Section, Aero-Physics Division. Associate AIAA.